Analysis and Optimization of the Axial Flux Permanent Magnet Synchronous Generator using an Analytical Method

Junaid Ikram[1], Nasrullah Khan[1], Qudsia Junaid[2], Salman Khaliq[3], and Byung-il Kwon[4]*

[1]COMSATS Institute of Information Technology, Islamabad, Pakistan
[2]National Transmission and Dispatch Company, Islamabad, Pakistan
[3]Intelligent Mechatronics Research Center, KETI, Korea
[4]Hanyang University, Ansan, Korea

This paper presents a 2-D analytical method to calculate the back EMF of the axial flux permanent magnet synchronous generator (AFPMSG) with coreless stator and dual rotor having magnets mounted on both sides of rotor yoke. Furthermore, in order to reduce the no load voltage total harmonics distortion (VTHD), the initial model of the coreless AFPMSG is optimized by using a developed analytical method. Optimization using the 2-D analytical method reduces the optimization time to less than a minute. The back EMF obtained by using the 2-D analytical method is verified by a time stepped 3-D finite element analysis (FEA) for both the initial and optimized model. Finally, the VTHD, output torque and torque ripples of both the initial and optimized models are compared with 3D-FEA. The result shows that the optimized model reduces the VTHD and torque ripples as compared to the initial model. Furthermore, the result also shows that output torque increases as the result of the optimization.

Keywords : axial flux permanent magnet synchronous generator, 2-D analytical method, no load voltage total harmonics distortion, Finite element analysis

1. Introduction

The axial flux Permanent magnet synchronous generator (AFPMSG) is suitable for low speed wind power generation due to its higher torque density [1, 2]. It has the advantages of a larger power to weight ratio and better cooling than radial flux topologies [3, 4]. Furthermore, the coreless stator topology of the AFPMSG reduces the generator weight and it has a lower cogging torque and unbalanced axial force [5, 6]. The coreless AFPMSG also has the advantage of high efficiency [7].

The computation of the air gap magnetic field distribution is important because it is required for the calculation of back EMF and torque. The computation of the magnetic field in an AFPMSG is done by using the magnetic equivalent circuit method, an analytical method for solving Maxwell's equations, or the finite element analysis (FEA). Although the FEA is more accurate com-

pared to the analytical method, due to the nonlinear fields in electrical machines, the effect of individual generator dimensions on the field distribution may not be easily identified and the method is very time consuming [8, 9]. Therefore, analytical methods are favored for finding a time-efficient solution.

The magnetic flux distribution in a PM machine is computed either by using a polar or rectangular coordinate system [10, 11]. Magnetic field computation of axial flux PM machines have been a focus of research in recent years. The field calculations of the double sided axial flux machine with slot-less stator are computed by representing magnets and coils as current sheets in [12]. An analytical method of the normal field component was developed for the single stator and rotor axial flux machine with flat multiple pole disc magnets by using the mean radius approach [13]. The magnetic field distribution of a single sided axial flux PM generator with a coreless stator has also been computed using the mean radius approach [14]. A voltage total harmonic distortion (VTHD) calculation of the single-sided coreless AFPMSG using a 2-D analytical method is presented in [14]. The optimization for the

*Corresponding author: Tel: +82-31-400-5165
Fax: +82-31-409-1277, e-mail: bikwon@hanyang.ac.kr

reduction in VTHD of the double sided AFPMSG using 3-D FEA is presented in [15]. However, an analytical solution of the magnetic field distribution of a coreless dual rotor single stator AFPMSG has not been presented yet, which uses the mean radius approach.

This paper presents a 2-D analytical method to optimize an AFPMSG having coreless stator and dual rotor yokes with PMs mounted on them. The developed analytical method is an extension of the analytical method developed in [14]. The analytical method presented in [14] is for coreless stator and sector shaped PMs are mounted on the inner side of one rotor yoke. Whereas, the developed analytical method presented in this paper is for coreless stator and sector shaped PMs are mounted on the inner side of both the rotor yokes. The equations are developed by using the same approach i.e. mean radius, rectangular coordinate system and solution of the Maxwell's equations as was presented in [14]. However, there is a minor difference in the derived equations and the equations that were presented in reference [14] due to the different position of lower and upper magnets from the reference point. In the developed analytical method equations are not being simply taken from the references [12-14] for the superposition but they are derived. Furthermore, developed analytical method is used for the optimization of the AFPMSG with coreless stator and PMs mounted on both sides of the rotor yokes. Optimization using the analytical method is done in order to reduce the time. Genetic algorithm and direct search method are employed on the developed analytical method for an optimal design of the AFPMSG. A transient 3-D FEA is used to verify the results of the developed 2-D analytical method for both the initial and optimized models. JMAG designer ver. 14.1 is used as a 3D-FEA tool in this paper. Performance comparison of AFPMSG's initial and optimized models under no load and load conditions is done with time stepping FEA. Due to dynamic behavior of the electric machines time stepping FEA is more accurate as compared to the magneto-static FEA. Furthermore time stepping FEA gives the results directly without recourse to further assumptions and calculations [16]. Finally, the VTHD, output torque and torque ripple of the initial and optimized models are compared using 3-D FEA.

The rest of this article is arranged as follows: Section II presents the 2-D analytical method for the modeling and analysis of coreless AFPMSGs. This is followed by Section III, which describes the optimization of the AFPMSG using the developed analytical method. In Section IV, a conclusion is drawn.

2. A 2-D Analytical Method for the Modeling and Analysis of Coreless AFPMSG

This section presents the 2-D analytical method for calculating the magnetic field density with Maxwell's equations using boundary conditions of the single coreless stator and dual rotor AFPMSG.

2.1. Initial Model

Figure 1 shows the initial model of the 1.0 kW, three phase, Y-connected, double-sided AFPMSG. The AFPMSG has two disc-shaped rotor yokes with permanent magnets placed on it. The coreless stator is sandwiched between two rotors and has stator windings fixed by the plastic resin. Three phases of the stator windings are arrayed periodically in the circumferential direction. Table 1 shows the design parameters of the AFPMSG for the 2-D
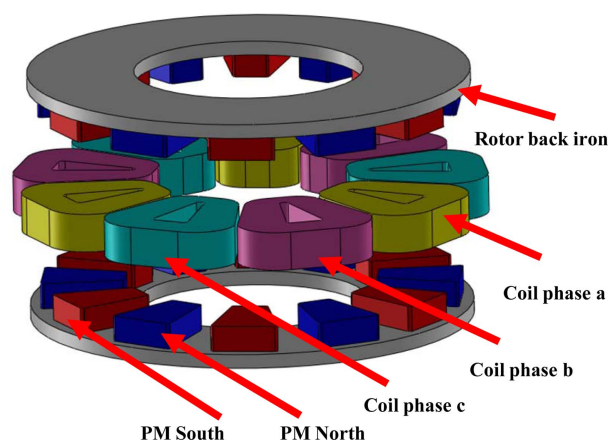
Fig. 1. (Color online) Exploded view of the 3-D FEA model of the AFPMSG.

Table 1. Parameters of the AFPMSG model.

Parameters	Units	Values
Outer radius of rotor	mm	81.2
Inner radius of rotor	mm	54.8
Height of back iron core	mm	4.0
Interpolar separation	mm	13.23
Height of magnet	mm	10.0
Height of machine	mm	46.0
Air gap	mm	1.5
Pole Pitch	mm	35.73
Speed	rpm	1100
No. of poles	-	12
Turns/phase	-	396
No. of coils	-	9

analytical method.

2.2. 2-D Analytical Method

For computation of the magnetic field, the mean radius approach and the rectangular coordinate system that is presented in [12-14] is used. Therefore, the 3-D geometry of the AFPMSG is converted into a 2-D linear model in which the X-axis represents the circumferential direction and the Y-axis represents the axial direction. The computation of the no load magnetic flux density components by the 2-D analytical method in the air gap and magnet regions is based on the solution of Maxwell's equations using the boundary condition method. In order to obtain the analytical solution and simplify the derivation of the analytical method, the following assumptions are made: There is no magnetic saturation and the rotor back iron has infinite permeability, the permanent magnets have uniform magnetization and have constant relative recoil permeability, and eddy currents are negligible.

To calculate the magnetic field by the individual rotor, one side's permanent magnets were neglected when calculating the magnetic flux density due to the other side's magnets. Furthermore, the coil region permeability is considered the same as the air gap region in the calculation of magnetic field due to upper and lower rotors magnets. The net magnetic field in the machine is the summation of magnetic fields due to both rotor permanent magnets. Figure 2 shows the AFPMSG linear model for the computation of the no load magnetic field due to the lower rotor permanent magnets. For permanent magnet machines with linear demagnetization characteristics, the Laplacian equation governs the scalar magnetic potential in both the air gap and permanent magnet regions [14]. The general solutions of the Laplacian equation in the air gap and magnet regions are given by Equations (1) and (2), respectively.

$$\varphi_I = \varphi_{III} = \sum_{n=1,3,5,\ldots}^{\infty} (D_1 e^{\frac{n\pi y}{\tau_p}} + D_2 e^{-\frac{n\pi y}{\tau_p}}) \cos(\frac{n\pi x}{\tau_p}) \qquad (1)$$
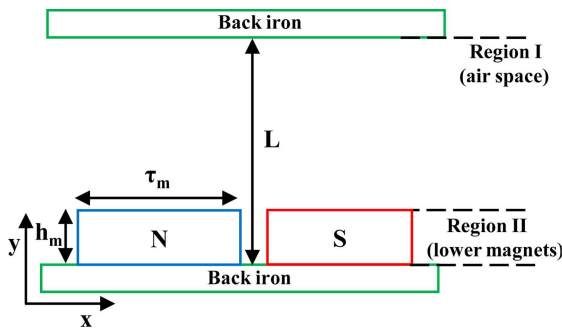

Fig. 2. (Color online) Linear representation of the AFPMSG for the lower rotor.

$$\varphi_{II} = \varphi_{IV} = \sum_{n=1,3,5,\ldots}^{\infty} (D_3 e^{\frac{n\pi y}{\tau_p}} + D_4 e^{-\frac{n\pi y}{\tau_p}}) \cos(\frac{n\pi x}{\tau_p}) \qquad (2)$$

Where φ is the magnetic scalar potential with subscripts represents regions, y is the axial height, τ_p is pole pitch, n is harmonic order and x is the circumferential distance.

The coefficients D_1 to D_4 in the above expressions are determined by imposing the boundary conditions. The magnetic field due to permanent magnets must satisfy the boundary conditions given in Equation (3) and (4) [11].

$$\begin{cases} H_{xI}(x,y)\big|_{y=0} = H_{xIII}(x,y)\big|_{y=0} = 0 \\ H_{xII}(x,y)\big|_{y=L} = H_{xIV}(x,y)\big|_{y=L} = 0 \end{cases} \qquad (3)$$

$$\begin{cases} B_{yI}(x,y)\big|_{y=L-h_m} = B_{yII}(x,y)\big|_{y=L-h_m} \\ H_{xI}(x,y)\big|_{y=L-h_m} = H_{xII}(x,y)\big|_{y=L-h_m} \end{cases} \qquad (4a)$$

$$\begin{cases} B_{yIII}(x,y)\big|_{y=L-h_m} = B_{yIV}(x,y)\big|_{y=L-h_m} \\ H_{xIII}(x,y)\big|_{y=L-h_m} = H_{xIV}(x,y)\big|_{y=L-h_m} \end{cases} \qquad (4b)$$

Where H_x is the circumferential components of the magnetic field intensity and B_y is the axial component of the magnetic flux density.

By employing the above mentioned boundary conditions, we get the values of the coefficients given by Equations (5-8).

$$D_1 = -\frac{M_n \tau_p}{2n\pi} \frac{\sinh(n\pi h_m / \tau_p)}{\Delta} \qquad (5)$$

$$D_2 = \frac{M_n \tau_p}{2n\pi} \frac{\sinh(n\pi h_m / \tau_p)}{\Delta} \qquad (6)$$

$$D_3 = \frac{M_n \tau_p}{2n\pi} \frac{\sinh(n\pi(L-h_m)/\tau_p)}{\Delta e^{n\pi L/\tau_p}} \qquad (7)$$

$$D_4 = -\frac{M_n \tau_p}{2n\pi} \frac{\sinh(n\pi(L-h_m)/\tau_p)}{\Delta e^{-n\pi L/\tau_p}} \qquad (8)$$

Here,

$$\Delta = \mu_r \cosh\left(\frac{n\pi h_m}{\tau_p}\right) \sinh\left(\frac{n\pi(L-h_m)/\tau_p}{\tau_p}\right)$$
$$+ \cosh\left(\frac{n\pi(L-h_m)}{\tau_p}\right) \sinh\left(\frac{n\pi h_m}{\tau_p}\right)$$

and,

$$M_n = 2\frac{B_r}{\mu_0} \alpha_p \frac{\sin(n\pi\alpha_p/2)}{n\pi\alpha_p/2}$$

Where h_m is axial length of the magnet, α_p is the pole arc to pole pitch ratio, L is the axial height of the machine, B_r is the residual flux density of the PM, μ_o is the perme-

ability of the free space and μ_r is the recoil permeability of the PM.

By substituting the above computed coefficients into Equations (1) and (2) and by solving for the magnetic field, we get the circumferential and axial components of the magnetic field. The magnetic field components due to the lower magnets in the air gap and magnet regions are given by Equations (9-12).

$$B_{xI} = \mu_0 H_{xI} = -\mu_0 \frac{\partial \varphi_I}{\partial x} = \mu_0 M_n \sum_{n=1,3,5,...}^{\infty} \frac{\sin(n\pi h_m/\tau_p)}{\Delta} \quad (9)$$
$$\sinh(n\pi y/\tau_p)\sin(n\pi x/\tau_p)$$

$$B_{yI} = \mu_0 H_{yI} = -\mu_0 \frac{\partial \varphi_I}{\partial y} = \mu_0 M_n \sum_{n=1,3,5,...}^{\infty} \frac{\sin(n\pi h_m/\tau_p)}{\Delta} \quad (10)$$
$$\cosh(n\pi y/\tau_p)\cos(n\pi x/\tau_p)$$

$$B_{xII} = \mu H_{xII} + \mu_0 M_x = -\mu \frac{\partial \varphi_{II}}{\partial x}$$
$$= \mu_0 M_n \sum_{n=1,3,5,...}^{\infty} \frac{\sin(n\pi(L-h_m)/\tau_p)}{\Delta} \quad (11)$$
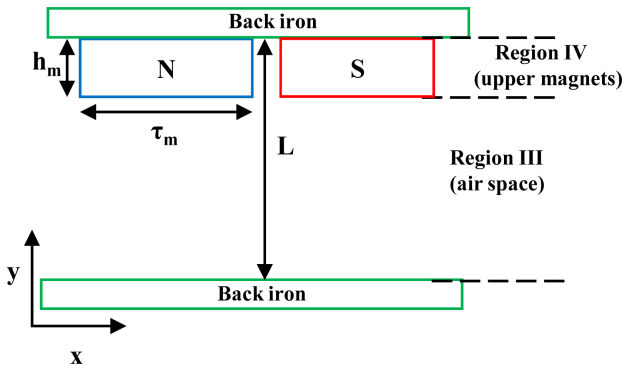$$\times \sinh(n\pi(L-y)/\tau_p)\sin(n\pi x/\tau_p)$$

$$B_{yII} = \mu H_{yII} + \mu_0 M_y = \mu_0 M_y - \mu \frac{\partial \varphi_{II}}{\partial y}$$
$$= \mu_0 M_n \sum_{n=1,3,5,...}^{\infty} \left\{ 1 - \frac{\mu_r \sin(n\pi(L-h_m)/\tau_p)}{\Delta} \right\} \cos(n\pi x/\tau_p) \quad (12)$$

Here,

$$\mu = \mu_0 \mu_r$$

Where B_x is the circumferential component of the flux density, B_y is the axial component of the flux density, H_x is the circumferential component of the field intensity and H_y is the axial component of the field intensity.

Figure 3 shows the linear model of the AFPMSG for

the computation of the no load magnetic field due to the upper rotor magnets. The circumferential and axial components of magnetic flux density due to upper rotor magnets in the air gap and magnet regions are given by Equations (13-16).

$$B_{xIII} = \mu_0 H_{xIII} = -\mu_0 \frac{\partial \varphi_{III}}{\partial x} = \mu_0 M_n \sum_{n=1,3,5,...}^{\infty} \frac{\sin(n\pi h_m/\tau_p)}{\Delta}$$
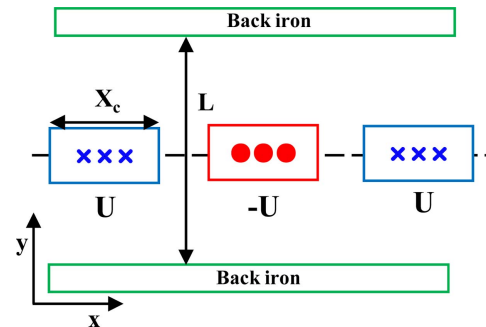$$\times \sinh(n\pi(L-y)/\tau_p)\sin(n\pi x/\tau_p) \quad (13)$$

$$B_{yIII} = \mu_0 H_{yIII} = -\mu_0 \frac{\partial \varphi_{III}}{\partial y} = \mu_0 M_n \sum_{n=1,3,5,...}^{\infty} \frac{\sin(n\pi h_m/\tau_p)}{\Delta}$$
$$\times \cosh(n\pi(L-y)/\tau_p)\cos(n\pi x/\tau_p) \quad (14)$$

$$B_{xIV} = \mu H_{xIV} + \mu_0 M_x = -\mu \frac{\partial \varphi_{IV}}{\partial x}$$
$$= \mu_0 M_n \sum_{n=1,3,5,...}^{\infty} \frac{\sin(n\pi(L-h_m)/\tau_p)}{\Delta} \quad (15)$$
$$\times \sinh(n\pi y/\tau_p)\sin(n\pi x/\tau_p)$$

$$B_{yIV} = \mu H_{yIV} + \mu_0 M_y = \mu_0 M_y - \mu \frac{\partial \varphi_{IV}}{\partial y}$$
$$= \mu_0 M_n \sum_{n=1,3,5,...}^{\infty} \left\{ 1 - \frac{\mu_r \sinh(n\pi(L-h_m)/\tau_p)}{\Delta} \right\} \cos(n\pi x/\tau_p) \quad (16)$$

The armature reaction refers to the magnetic field produced by currents in the stator coils and their interaction with the field flux. The disc armature winding is considered as thin current sheets. Figure 4 shows the linear model of the AFPMSG for the computation of the armature reaction field. The axial component of the armature reaction is given by Equation (17) [3].

$$B_y = \mu_0 \hat{K}_n \left[\frac{\cosh(npL/2R)}{\sinh(npL/R)} \right] \cosh(np(L-y)/R)\cos(npx/R) \quad (17)$$

Fig. 3. (Color online) Linear representation of the AFPMSG for the upper rotor.

Fig. 4. (Color online) Linear representation of the AFPMSG coil region by current sheet.

For computing the B_{eff}, the effect of both the radius R and axial position y are considered. These variables are considered because the air gap flux density is varied with the radial position R for a specific axial position y. The effective value of the no load flux density B_{eff} is given by Equation (18).

$$B_{eff} = \frac{1}{(R_2 - R_1)(y_2 - y_1)} \int_{R_1}^{R_2} \int_{y_1}^{y_2} K_{wn} B(R, y) dR dy \qquad (18)$$

Here, $B(R, y)$ is the sum of the axial and circumferential components of the no load magnetic field due to the lower and upper magnets in the coil or air gap region, K_{wn} is the winding factor, R_1 and R_2 are the inner and outer radii of the rotors and y_1 and y_2 are the axial positions of lower and upper surfaces of the coil region.

The back EMF is computed by considering the axial and circumferential components of twin rotor magnets. The back EMF E_b in the air gap is given by Equation (19).

$$E_b = \sqrt{6} \frac{f T_{ph}}{p} (R_2^2 - R_1^2) B_{eff} \qquad (19)$$

where T_{ph} the number of turns per phase.

2.3. Characteristics Analysis

The axial and circumferential components of the magnetic flux density due to the lower and upper magnets in the air gap region are shown in Fig. 5(a) and Fig. 5(b), respectively. The results show that the axial and circumferential components of magnetic flux density due to the lower magnet decrease as y increases up to the center of the coil, i.e., 19 mm. The result also shows that the axial and circumferential components of the magnetic flux density due to upper magnets increase as y increases from the center of the coil, i.e., 19 mm.

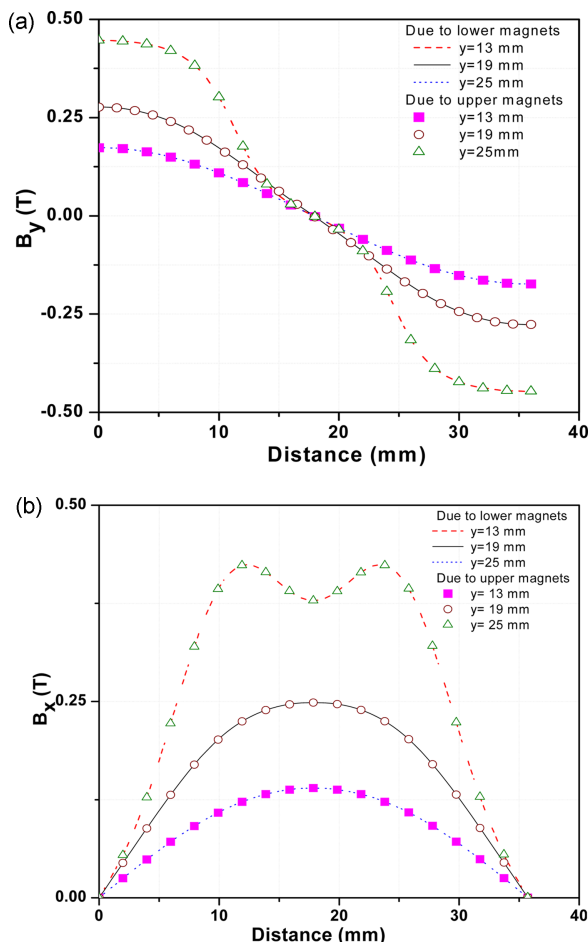The axial and circumferential components of the mag-

Fig. 5. (Color online) (a) Axial component of the field in the air gap (b) Circumferential component of the field in the air gap.
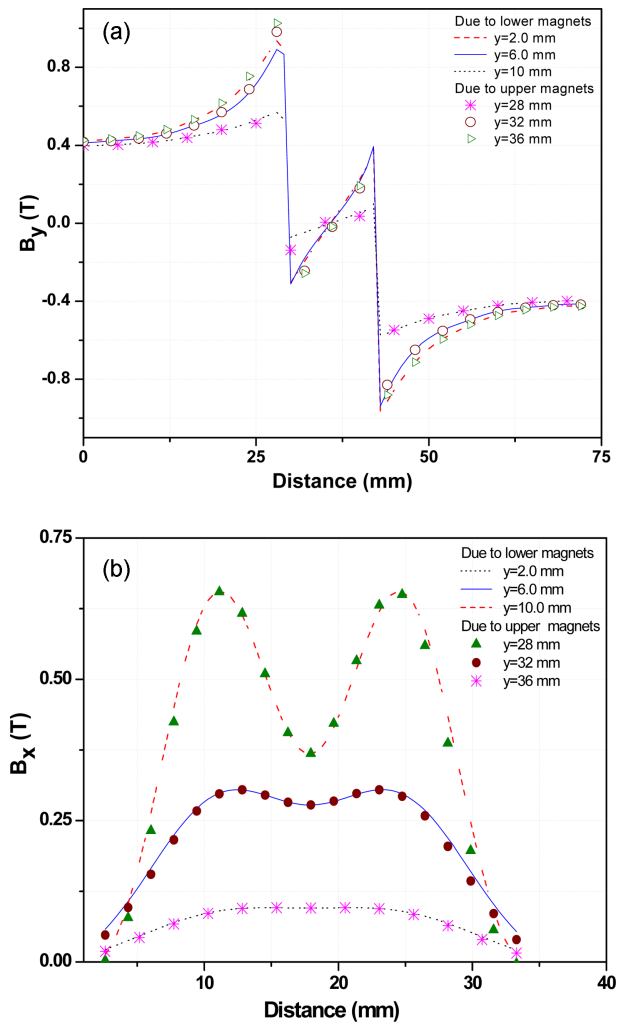

Fig. 6. (Color online) (a) Axial component of the field in the magnet regions. (a) Circumferential component of the field in magnet regions.
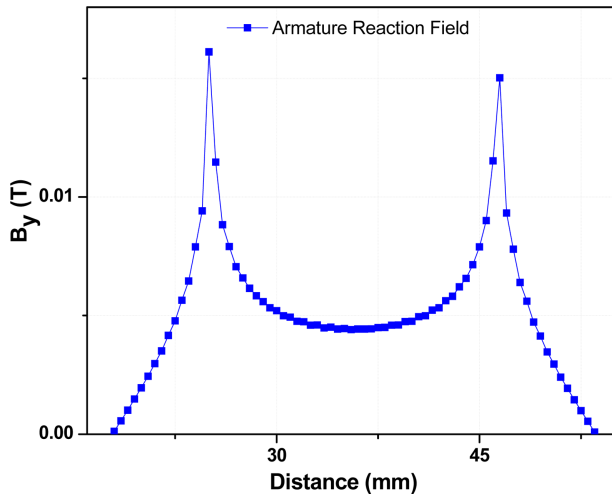
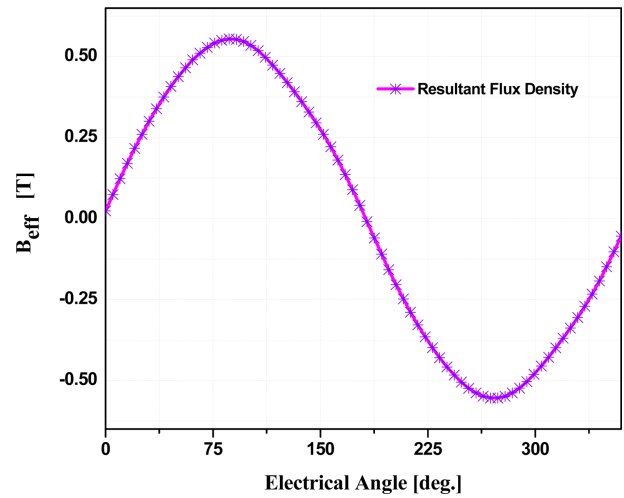**Fig. 7.** (Color online) Armature reaction field.

Fig. 8. (Color online) Resultant magnetic field.

netic flux density due to the lower and upper magnets in the magnet region are shown in Fig. 6(a) and Fig. 6(b), respectively. The results show that the axial and circumferential components of the magnetic flux density due to the lower magnet increase as y increases up to the magnet surface. The results also show that the axial and circumferential components of the magnetic flux density due to the upper magnet decrease as y increases from the surface of the magnet.

The axial component of the resultant armature reaction at the mean axial position (air gap region) at the rated current for 7 Arms is shown in Fig. 7, by using Equation (17). The armature reaction magnetic field is highest at the edges of the phase band. Also the result shows that the resultant armature reaction field is very small compared to the no load magnetic field, and hence can be ignored. The resultant magnetic field is computed by adding the axial and circumferential components of the magnetic field due to the upper and lower magnets. The resultant magnetic field is shown in Fig. 8. The computed resultant magnetic field is at the mean radius and axial height.

The back EMF is computed by using Equation (19). The calculated back EMF is at the mean radius and axial height. The computational time for the back EMF using the analytical method is less than one minute, whereas as it is around 15 hours using 3-D FEA. Thus, the analytical method shows rapid characteristics analysis. The back EMFs computed by using the 2-D analytical method and 3-D FEA are shown in Fig. 9. The back EMFs computed by using both the analytical method and the 3-D FEA are almost equal. The back EMF fundamental harmonic component is 92 % and 90.6 % using the analytical method and 3-D FEA, respectively. Table 2 shows the
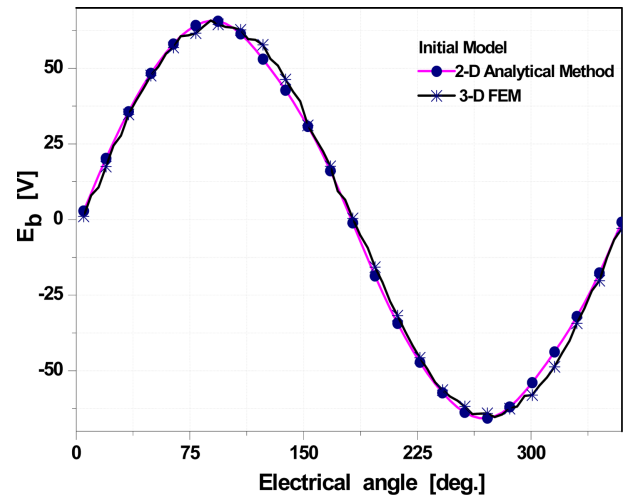

Fig. 9. (Color online) Comparison of back EMF by 2-D analytical method and 3-D FEA of the initial model.

Table 2. 2-D analytical and 3-D FEA performance comparison of the initial model.

Parameters	Units	2-D Analytical Method	3-D FEA
back EMF	Vpeak	65.7	65.3
VTHD	%	2.5	3.15

summary of the results obtained using the 2-D analytical model and 3-D finite element analysis (FEA). The VTHD is higher for the 3-D FEA analysis because it considers the nonlinear field characteristics.

3. Optimization of the AFPMSG using 2-D Analytical Method
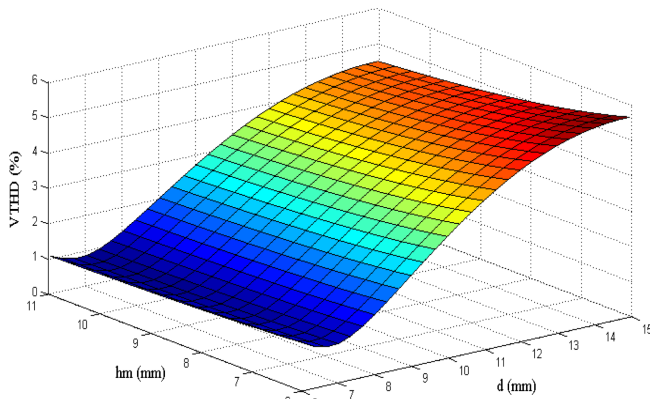
The VTHD varies with the d and h_m, as shown in Fig.

Fig. 10. (Color online) VTHD trend.

Fig. 12. Optimal design process.

10. The VTHD is calculated by computing the back EMF using the 2-D analytical method. It is clear from Fig. 10 that the VTHD increases rapidly as the interpolar separation between the magnet increases. The VTHD also varies with the height of the magnet, but this variation is significantly smaller in comparison.

The optimization of the VTHD % is made with the design variable, interpolar separation, d, and axial height of magnets, h_m, while maintaining the back EMF > 65 V_{peak}. Figure 11 shows the selected design variable and their optimal values. For the initial model under consideration, h_m is equal to 10.0 mm and d is equal to 13.23 mm. An optimal design process employing a developed 2-D analytical method is shown in Fig. 12. The genetic algorithm (GA) and direct search methods are utilized to find the optimized values of the selected design variables and objective functions.

The VTHD has a value of 2.5 % for the initial model by 2-D analytical method. At the optimized values of d and h_m provided by the GA and direct search method, the VTHD reduces to 0.39 %. The VTHD % is also computed using 3-D FEA. The result shows that a considerable
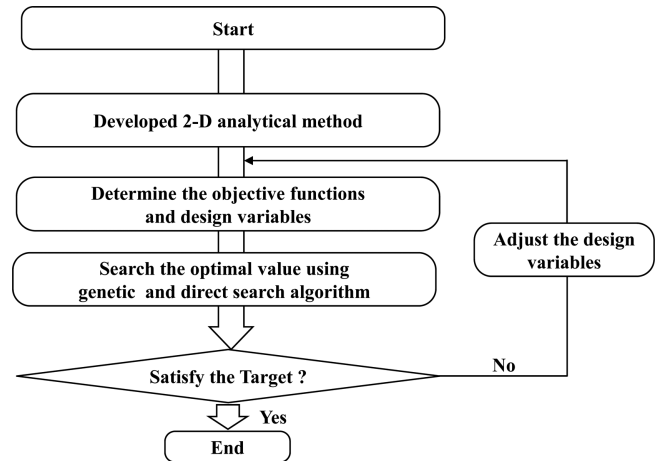
reduction in the VTHD is obtained as the result of optimization using the analytical method in the optimized model. The VTHD has a value of 3.15 % and 1.5 % for the initial and optimized models using FEA. The percentage decrease achieved in VTHD is 52.38 % as the result of the optimization using analytical method. Since the 3-D FEA considers the nonlinear characteristics, the VTHD is slightly and consistently higher than the analytical method results.

The back EMF of the optimized model, computed by the 2-D analytical method, is compared with 3-D FEA, as shown in Fig. 13. The result shows that the backs EMF of both the analytical and 3-D FEA are consistent. The analysis of the back EMF waveforms is performed to determine the VTHD and fundamental harmonic component. Figure 14 shows the comparison of the harmonic components of the initial and the optimized models using 3-D FEA. Since the considered AFPMSG is Y-connected, only the comparison of belt harmonics is considered in this paper. The result shows that the optimized model has an increased fundamental harmonic component. The result
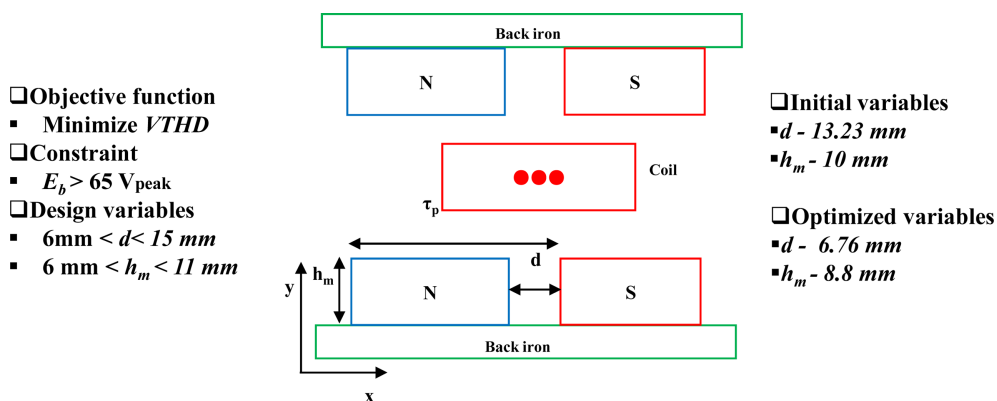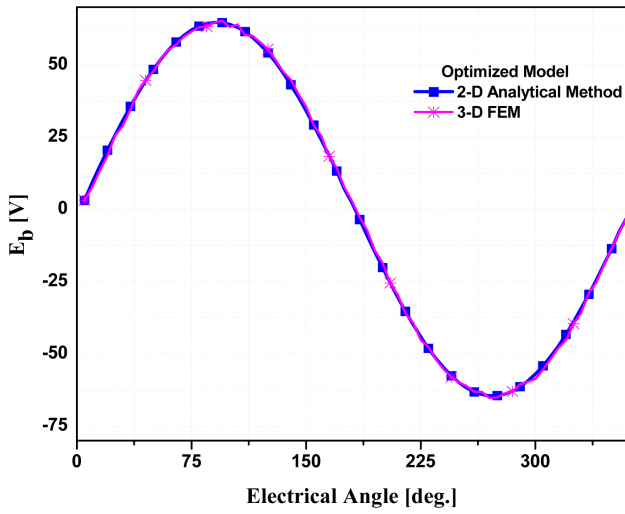

Fig. 11. (Color online) Selected design variables and their optimal values.
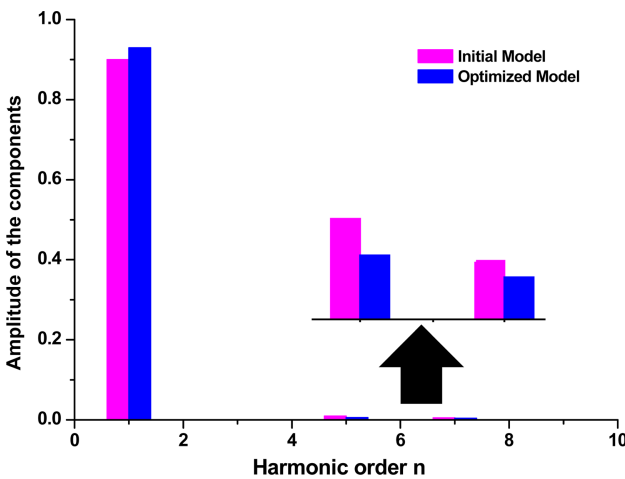
Fig. 13. (Color online) Comparison of the back EMF by 2-D analytical method and 3-D FEA for the optimized model.

Fig. 14. (Color online) Belt Harmonics comparison.

Table 3. 2-D analytical and 3-D FEA performance comparison of the optimized model.

Parameters	Units	2-D analytical method	3-D FEA
back EMF	Vpeak	65.5	65.4
VTHD	%	0.39	1.5

Table 4. Comparison of the initial and optimized model.

| Parameters	Units	Initial Model	Optimized Model
Interpolar separation	mm	13.23	6.76714
Height of magnet	mm	10.0	8.81239
Axial height of machine	mm	46	43.62
back EMF	V	65.3	65.4
VTHD	%	3.15	1.5
Torque	Nm	6.9	7.74
Torque ripple (T_{pk2pk})	%	45	36

also shows the reduction in belt harmonics components. Performance comparison of the optimized model using the 2-D analytical method and 3-D FEA is shown in Table 3. The result shows that the back EMF of the optimized model using 2-D analytical method and 3-D FEA are almost the same. The back EMF fundamental harmonic component is 93 % and 92 % using the analytical method and 3-D FEA, respectively. Finally, the comparison of the initial design and the optimized design of the AFPMSFG is tabulated in Table 4. The back EMF of the initial and optimized model is almost the same. The percentage decrease in the VTHD is 52.38 % as a result of the optimization. Also the optimized model is more compact in comparison to the initial model.

In order to obtain a load analysis of the AFPMSG's initial and optimized models, a load resistor of 6.8 ohms
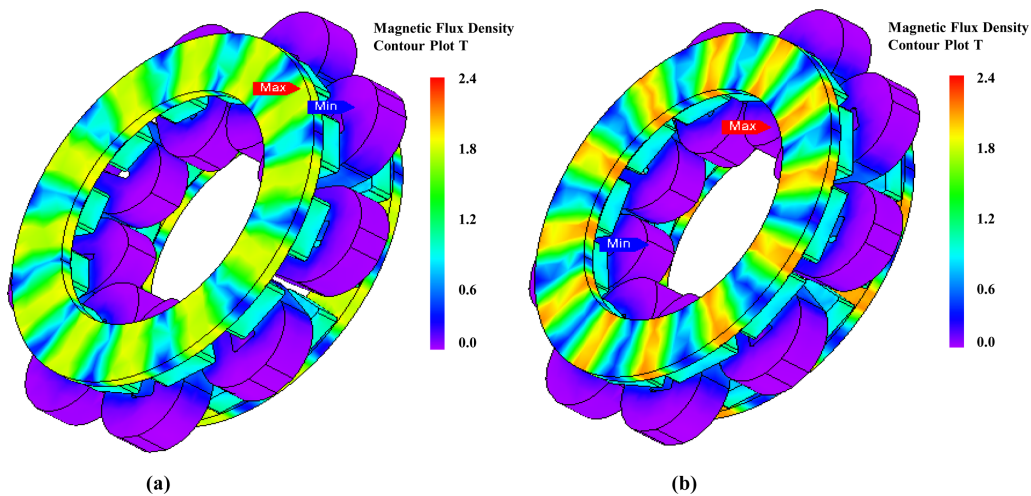
Fig. 15. (Color online) Flux density distribution plots by 3D-FEA: (a) Initial model (b) Optimized model.
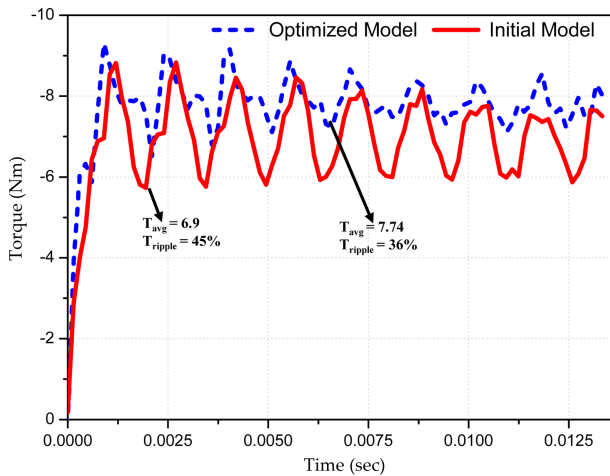
Fig. 16. (Color online) Torque comparison of the initial and optimized model by 3D- FEA.

is connected across each phase. The flux density distribution of the initial and optimized models under loaded condition is shown in Fig. 15(a) and Fig. 15(b), respectively. The maximum flux density (B_{max}) is almost 1.8 T and 2.0 T for the initial and optimized models respectively, which occurs at the rotor back iron. The increased flux density of the optimized model is due to its increased surface area of the magnet due to the decreased interpolar separation as can be seen from the Table 4.

An improvement in the output torque of the optimized model is obtained, as compare to the initial model. A comparison of the output torque of the initial and optimized models is shown in Fig. 16. The output torque of the initial model is 6.9 Nm and that of the optimized model is 7.74 Nm. Furthermore, a reduction in the torque ripple of the optimized model is achieved. The torque ripple of the initial model is 45 % and that of the optimized model it is 36 % by 3D-FEA.

4. Conclusion

This paper presents a 2-D analytical method to compute the back EMF of the coreless dual rotor AFPMSG by solving Maxwell's equations considering boundary conditions. The results of the 2-D analytical method are verified with 3-D FEA. Furthermore, the VTHD % is reduced through optimization with the developed 2-D analytical method. The VTHD of the initial model is compared with the optimized model using 3-D FEA and results show that the VTHD is 1.5 %, which is a considerable improvement over the previous 3.15 %. Furthermore, the optimal design exhibits reduced torque ripple with higher average output torque, as compare to the initial model. The time saved due the 2-D analytical method proves the advantages of the analytical technique against the time-consuming 3-D FEA method.

References

[1] Asko Parviainen, Ph.D. Thesis, University of Technology Lappeenranta, Finland (2005).
[2] Y. Chen, P. Pillay, and A. Khan, IEEE Trans. Ind. Appl. **41**, 6 (2005).
[3] Solmaz Kahourzade, Amin Mahmoudi, and Hew Wooi Ping, Canadian Journal of Electrical and Computation Engineering **37**, 1 (2014).
[4] Metin Aydin, Ph.D. Thesis, University of Wisconsin-Madison, (2004).
[5] Chang-Chou Hwang, Ping-Lun Li, Frazier C. Chuang, Cheng-Tsung Liu, and Kuo-Hua Huang, IEEE Trans. Magn. **45**, 3 (2009).
[6] W. Fei, P. C. K. Luk and K. Jinupun, IET Electric Power Appl. **4**, 9 (2010).
[7] Bing Xia, Jian-Xin Shen, Patrick Chi-Kwong Luk, and Weizhong Fei, IEEE Trans. Ind. Electron. **62**, 2 (2015).
[8] A. B. Proca, A. Keyhani, and A. EL-Antably, IEEE Trans. Energy Convers. **18**, 3 (2003).
[9] P. Virtic, P. pisek, T. Marcic, M. Hadziselimovic, and B. Stumberger, IEEE Trans. Magn. **44**, 11 (2008).
[10] Z. Q. Zhu, D. Howe, E. Bolte, and B. Ackermann, IEEE Trans. Magn. **29**, 1 (1993).
[11] E. P. Furlani, Permanent Magnet and Electromechanical Devices, Academic Press, New York (2001) pp. 470-479.
[12] J. R. Bumby, R. Martin, M. A. Muller, E. Spooner, N. L. Brown, and B. J. Chalmers, IEEE Proc. Power Appl. **151**, 2 (2004).
[13] E. P. Furlani, IEEE Trans. Magn. **30**, 5 (1994).
[14] T. F. Chan, L. L. Lai, and S. Xie, IEEE Trans. Energy Convers. **24**, 1 (2009).
[15] Yong-min You, Hai Lin, and Byung-il Kwon, JEET **7**, 1 (2012).
[16] Richard Martin, Ph.D. Thesis, University of Durham, (2007).